Article:
Tanaka, M, Hayashi, M, Roach, L et al. (2021) Synthesis of near-infrared absorbing triangular Au nanoplates using biomineralisation peptides. Acta Biomaterialia, 131. pp. 519-531. ISSN: 1742-7061

https://doi.org/10.1016/j.actbio.2021.06.010

Synthesis of near-infrared absorbing triangular Au nanoplates using biomineralisation peptides

Masayoshi Tanaka[a,*], Mirei Hayashi[a], Lucien Roach[b], Yuka Kiriki[a], Tetsuya Kadonosono[c], Takahiro Nomoto[d], Nobuhiro Nishiyama[d], Jonghoon Choi[e], Kevin Critchley[b], Stephen D. Evans[b], and Mina Okochi[a,*]

[a]*Department of Chemical Science and Engineering, Tokyo Institute of Technology, 2-12-1-S1-24, O-okayama, Meguro-ku, Tokyo 152-8552, Japan*

[b]*School of Physics and Astronomy, University of Leeds, Leeds LS2 9JT, United Kingdom*

[c]*School of Life Science and Technology, Tokyo Institute of Technology, 4259, Nagatsuta, Midori-Ku, Yokohama, Kanagawa 226-8501, Japan*

[d]*Laboratory for Chemistry and Life Science, Institute of Innovative Research, Tokyo Institute of Technology, 4259, Nagatsuta, Midori-Ku, Yokohama, Kanagawa 226-8501, Japan*

[e]*School of Integrative Engineering, Chung-Ang University, Seoul 06974, Korea*

***Corresponding author:**

M. Okochi,

Department of Chemical Science and Engineering, Tokyo Institute of Technology, 2-12-1, O-okayama, Meguro-ku, Tokyo 152-8552, Japan

Tel/Fax: +81-(0)3-5734-2116; E-mail: okochi.m.aa@m.titech.ac.jp

M. Tanaka,

Department of Chemical Science and Engineering, Tokyo Institute of Technology, 2-12-1, O-okayama, Meguro-ku, Tokyo 152-8552, Japan

Tel/Fax: +81-(0)3-5734-2140/+81-(0)3-5734-2116; E-mail: tanaka.m.bn@m.titech.ac.jp

Abstract

Triangular Au nanoplates (TrAuNPls) possessing strong plasmonic properties can be used as photothermal agents in cancer therapy. However, the preparation of such controlled morphologies typically requires harsh synthetic conditions. Biomolecules offer an alternative route to developing biocompatible synthetic protocols. In particular, peptides offer a novel route for inorganic synthesis under ambient conditions. Herein, using the previously isolated peptide, ASHQWAWKWE, for Au nanoparticle (AuNP) synthesis, the conditions for preparing TrAuNPls via a one-pot synthetic process of mixing $HAuCl_4$ and peptides at room temperature were investigated to effectively obtain particles possessing near-infrared absorbance for non-invasive optical diagnosis and phototherapy. By adjusting the peptide concentration, the size and property of TrAuNPls were controlled under neutral pH conditions. The synthesised particles showed potential as photothermal therapeutic agents *in vitro*. In addition, peptide characterisation using B3 derivatives revealed the importance of the third amino acid histidine in morphological regulation and potential circular Au nanoplates (AuNPl) synthesis with ASEQWAWKWE and ASAQWAWKWE peptides. These findings provide not only an easy and green synthetic method for TrAuNPls and circular AuNPls, but also some insight to help elucidate the regulation of peptide-based nanoparticle synthesis for use in cancer therapy.

Keywords: Mineralisation peptide, Triangular nanoplate, Gold nanoparticle, Photothermal therapy

1. Introduction

Controlled synthesis of Au nanoparticles (AuNPs) has been an active and dynamic research field because of their potential applications owing to the unique optical properties, efficient photothermal conversion, low cytotoxicity, and high stability, especially in biomedical applications such as bioimaging and cancer hyperthermia [1,2]. AuNPs have strong absorbance peaks in the visible and near-infrared (NIR) wavelength range emanating from their localised surface plasmonic resonance (LSPR), the peak absorbance wavelengths of which can be tuned by controlling the particle morphology. A variety of AuNP morphologies, such as spheres, rods, and plates have been investigated [3]. Among them, Au nanorods, nanoshells, and nanoplates (AuNPls) have attracted particular attention in biological applications owing to their strong NIR absorbance, because NIR light (650–850 nm) is able to efficiently penetrate biological tissues [4–7]. Such AuNPs can be illuminated *in vivo* and act as efficient nanosized cell heating agents for photothermal therapy. However, the synthesis of such materials currently requires complex synthetic methods and harsh reagents [1,2]. The most popular synthetic methods for Au nanorods and triangular AuNPls (TrAuNPls) require the use of surfactants, such as hexadecyltrimethylammonium halides [8,9]. Although these methods can precisely regulate the morphology of AuNPs, hexadecyltrimethylammonium is highly cytotoxic [10,11], and great efforts must be put into removing it from the synthesised particles before biological application [7].

Considerable research has been focused on developing more eco-friendly protocols to produce these particles [12–14]. Among the various methods, biomineralisation, a method that uses biological molecules to generate inorganic nanomaterials from metallic salts having highly controlled structures at the nanoscale, has drawn researchers' attention as a potential synthetic route which can be achieved under ambient conditions [15–17]. Various biomolecules can act as shape-directing agents during syntheses by regulating the growth of specific crystal facets and encouraging particle growth in specific directions [18–20]. Among them, peptides are promising candidate molecules because of their relatively small molecular size and stability that can bind not only metal ions, but also metallic crystals. The

diverse functionalities can be designed and tuned abundantly by combining amino acids with various physicochemical properties through chemical synthesis [21–25].

Using various peptide-screening techniques (e.g., phage and cell surface display libraries), a series of peptides that strongly bond to various metallic nanoparticles, including AuNPs, have been isolated and utilised as templates for particle synthesis [26–29]. In contrast, some types of peptides, named mineralisation peptides, exhibit catalytic properties for nanoparticle synthesis without any additional reducing agents, such as $NaBH_4$ [21–23]. These mineralisation peptides are generally screened from peptides that strongly bind to target crystals. Considering the chemical equilibrium between crystalline nanoparticles and metal ions in a solution, it has been suggested that the strong binding of peptides stabilises the crystals, resulting in a shift in the equilibrium from an ionic state towards a crystalline state. As it is known that crystal-binding molecules potentially regulate crystal morphology [29–31], a bi-functional peptide leading to both binding of Au surfaces and Au(III) reduction offers a biomolecular method of producing morphology-regulated nanoparticles. A few biomineralisation peptides for producing unique AuNP morphologies (e.g., hexagonal plate, spherical, and nanoribbons) have been reported previously [32,33]. However, selectively controlling the particle morphology and properties, especially for achieving NIR absorbance by AuNPs, has not yet been reported.

Recently, we succeeded in identifying over 100 peptides as Au mineralisation peptides from a library of 200 AuNP binding peptides using peptide array technology [22,34]. This method allows the exploration of large numbers of peptide sequences, identifying those that effectively mineralise AuNPs, and can be used to screen peptides which produce AuNPs with specific optical properties through peptide array imaging after mineralisation. By grouping peptides based on the observed colour produced on the peptide array post-mineralisation, a mineralisation peptide named B3 (originally named Au nanoparticle binding peptide, AuP40; ASHQWAWKWE), was identified from a list of peptides producing blue coloured AuNPs. B3 is capable of mineralising decahedral AuNPs and TrAuNPls via a one-pot synthesis under mild aqueous conditions. Therefore, we investigated the conditions conducive to synthesising TrAuNPls using the B3 peptide and diversity in the morphology of these synthesised particles by B3

peptide derivatives, as well as their potential application as photothermal conversion agents. Our findings could potentially provide an easy method for controlled production of nanomaterials with biological applications, especially in cancer therapy.

2. Materials and methods

2.1. Evaluation of AuNP biomineralisation using peptides

Peptides were synthesised following the standard fluorenylmethoxycarbonyl (Fmoc) based solid-phase protocol with a Respep SL automatic peptide synthesizer (Intavis Bioanalytical Instruments AG, Germany), as previously described [35,36]. Briefly, Fmoc-protected amino acid residues were applied to the TentaGel Resin in a stepwise manner for elongation of the peptide chain. The synthesised peptides were deprotected with 20% piperidine in *N,N*-dimethylformamide and cleaved from the scaffold resin using a cleavage cocktail containing trifluoroacetic acid, water, thioanisole, phenol, ethanedithiol, and triisopropylsilane (82.5:5:5:2.5:1). Peptides were precipitated in cold diethyl ether and dissolved in 30% acetonitrile for storage as freeze-dried powder. Purification was performed with an ODS-80TS column (Tosoh Corp., Tokyo, Japan) and a high-performance liquid chromatography (HPLC) system (LC-20AR, CBM-20A, SIL-20AC, CTO-20AC, SPD-20AV, Shimadzu Corp., Kyoto, Japan) before measuring the molecular weight by matrix-assisted laser desorption/ionization mass spectrometry (AXIMA-CFRPlus, Shimadzu Corp.). The final purity of the peptides was confirmed to be >85% using an ODS-100Z column (Tosoh Corp.) and an HPLC system (Shimadzu Corp.).

All purified peptides were dissolved in 100% dimethyl sulfoxide to form a 100 mM peptide solution and added to Tris-buffered saline (7.0 mM Tris, 21 mM NaCl, pH 7.4). The biomineralisation reaction was initiated at 25°C by the addition of $HAuCl_4$ (final concentration: 0.5 mM). To avoid evaporation, a layer of silicone oil was added above the reaction solution. Transmission electron microscopy (TEM) analysis was conducted using a Hitachi H7650 microscope (Hitachi, Tokyo, Japan) at a working voltage of 100 kV. The specimens were prepared by drop-casting 1.5 µL of the sample dispersion onto a formvar-coated 200-mesh Cu grid. Field emission scanning electron microscopy was

conducted with an S5500 microscope (Hitachi) at 15 kV using the same Cu grid. Extinction of the AuNPs in the UV-visible range was measured using a microtiter plate reader (PowerScan 4, DS Pharma Biomedical Co., Ltd., Osaka, Japan).

2.2. Evaluation of effects of the pH and buffer on biomineralisation of AuNPls with NIR absorbance

The difference in the pH and ion content of the reaction solution for AuNP synthesis using the B3 peptide was evaluated using the different buffers listed in Table 1, which were prepared according to previously reported recipes and diluted to the required concentration [37]. As the acidic condition may help to promote crystal growth by the peptide [32], the pH range for the evaluation was set from pH 1.0 to neutral pH of 7.4, in this study. According to the results obtained using the same concentration of different buffers, the AuNP synthesis was evaluated with different concentrations of HCl-KCl buffer (pH 1.6) and Tris-buffered saline (TBS) (pH 7.4) from 0 to 50 mM and from 25 to 200 mM, respectively. Extinction (400–950 nm) was measured after 24 h (PowerScan 4, DS Pharma Biomedical Co., Ltd.). The samples were observed by TEM as described earlier. The B3 peptide concentration dependency (0, from 0.10 to 0.30 with 0.02 pitches, 0.50, and 1 mM) was also evaluated in 7 mM TBS buffer. After 24 h of reaction, UV-visible spectra were obtained. The position of the second peak was extracted from the spectrum by differentiating each UV-visible spectrum in OriginPro (OriginLab, USA) and locating the points of inflection. TEM observations of more than 200 randomly selected particles were conducted and the size distributions (± standard deviation (SD)) based on the Feret diameter were evaluated using ImageJ software.

2.3. Surface analysis of biomineralised AuNPls with NIR absorbance using X-ray photoelectron spectroscopy

X-ray photoelectron spectroscopy (XPS) was performed with an ESCAlab 250 (Thermo Fisher Scientific) using a monochromated Al K-α source operated at 15 kV and 10 mA, with a spot diameter of approximately 0.5 mm^2. Samples of AuNPs synthesised by the B3 peptide were prepared by drop-casting

onto an indium substrate. The substrate was electrically grounded to the analyser during acquisition. Survey scans were performed using pass energy of 150 eV, a step size of 1 eV, and a dwell time of 200 ms. High-resolution scans of the selected binding energy ranges were used for detailed analysis. The detailed scans were collected using pass energy of 20 eV, a step size of 0.1 eV, and a dwell time of 200 ms. The number of scans was adjusted to maintain a satisfactory signal-to-noise ratio for all data. All data were collected using a 90° take-off angle. To correct for any charging effects, all XPS data were normalised to the predominant C 1s peak at 284.6 eV. Background correction was applied using the Shirley background algorithm. Pseudo-Voigt functions were used to fit the peaks in the high-resolution scans and the Wagner database for sensitivity factors was used to determine the relative atomic percentage of each element.

2.4. Cell viability assay

Normal Human Dermal Fibroblast (NHDF, ATCCPCS-201-012) cells were seeded at a population of 1.0 × 10^3 cells per well in a 96-well plate. The cells were incubated for 3 hours and reached 40% confluence. The spent media were replaced with test nanoparticles of (0, 2.5, 5, 10, 20 40 and 80 µg/mL) concentrations mixed with 100 µL of fresh media. The plates were then incubated for 24 hrs at 37°C in a humidified incubator with a 5% CO_2 environment. Following the incubation periods, the medium was removed and the cells were co-stained with calcein AM (final conc.: 1 µM) and propidium iodide (PI, final conc.: 0.5 µM) for 15 min. After removing the staining solution, fresh media without phenol red (100 µL) was added prior to the fluorescent imaging.

2.5. Evaluation of the photothermal effect of biomineralised AuNPs in vitro

The temperature transition was observed using a xenon lamp (MAX-303, Asahi Spectra, Co., Ltd., Tokyo, Japan) and longpass filter that cut the short wavelength (LVX610, $\lambda \geq 610$ nm) to irradiate a 2 mL sample (300 mW/cm^2, 1.0 × 10^{14} particles/mL) of B3-AuNPs synthesised using three different peptide concentrations (0.20, 0.24, and 0.28 mM) and a control with no peptide in a 1 cm square cuvette.

The temperature increases during the light irradiation were recorded every 30 s using a digital thermometer.

HeLa cervical adenocarcinoma cells (JCRB9004; JCRB Cell Bank, Osaka, Japan) were cultured in Dulbecco's Modified Eagle Medium supplemented with 10% fetal bovine serum (FBS) and 1% penicillin/streptomycin in 6 cm dishes placed in a humidified 5% CO_2 incubator at 37 °C. Cells were split at approximately 80% confluence via trypsinisation. The cells (1.0×10^6, 1 mL) were added to the AuNP solution synthesised with the B3 peptide (0.24 mM, 1 mL), and irradiated for 5 min using a xenon lamp (1.8 W/cm^2). The photothermal effect on HeLa cells was evaluated by fluorescent microscopy using a live/dead cell staining kit (LIVE/DEAD™ Fixable Red Dead Cell Stain Kit for 488 nm excitation, L23102; Thermo Fisher Scientific, Tokyo, Japan). Red and green staining confirmed dead and live cells, respectively.

2.6. Finite element method (FEM) simulation of AuNPs

The optical response of AuNPs were simulated using COMSOL's radio frequency module. Calculations were performed in the frequency domain in the scattered field formulation using the PARDISO direct solver. Refractive index values for Au were taken from previous literature [38]. Particles were simulated in medium of water ($n = 1.333$) surrounded by a perfectly matched layer. σ_{abs} was calculated through a volume integral of the resistive heat losses inside the AuNP, Q_{rh}. σ_{scat} was calculated through a surface integral of the Poynting vector, at the particle surface.

2.7. Statistical analysis

All TEM images were analysed with ImageJ software. All results were expressed as mean ± standard deviation.

3. Results

3.1. Effects of the pH and buffer on AuNPl biomineralisation with NIR absorbance

To evaluate the buffer and pH effects on AuNP synthesis using the B3 peptide, six different buffers (pH 1.0–7.4) (Table 1) were used, and the UV-visible spectra measured after AuNP synthesis. Five of these buffers spanned the whole pH range in sequence (HCl-KCl, Gly-HCl,HOAc, PO_4,TBS), whilst the sixth, the Cit-PO_4 buffer, spanned pH 2.8 – 6.4 covering pH values also covered by the Gly-HCl, HOAc, and PO_4 buffers allowing some comparison of the impact of ion content at these pH values (Fig. 1a, 1b and supplementary Fig. S1). Fig. 1a presents a microtiter plate after AuNP synthesis using the B3 peptide in these buffers. It can be seen that the observed colour changes correlate more closely with the buffer used, more than the pH. Particles synthesised in HCl-KCl buffers (pH 1–2.2) produced purple-coloured solutions. This blue hue is indicative of absorbance in the red region of the spectrum, which is typically only achievable through the formation of particles with more complex morphologies than spheres. The UV-visible spectra of these solutions agreed with the broad-spectrum absorbance extending towards the NIR region (Fig. 1b). The solution synthesised at pH 1.0 also had a shoulder centred at ~650 nm, suggesting an additional plasmonic mode not present for spherical AuNPs, which show a typical peak at ~530 nm. In the case of Gly-HCl (pH 2.8–3.4), dark red solutions were produced, and the spectra for these solutions showed a single peak at ~530 nm with no absorbance in the NIR region, suggesting the formation of spheres alone. Furthermore, both HOAc (pH 4.0–5.2) and PO_4 buffers (pH 5.8–7.0) exhibited reduced mineralisation of the gold salt, producing turbid, slightly red solutions, with only the HOAc buffer at pH 4 showing a strong red colour. The spectra obtained for all these solutions showed a single peak at ~530 nm, suggesting a population of mostly spheres.

By comparison, the Cit-PO_4 buffer (pH 2.8 – 6.4), which overlapped the buffering ranges of the Gly-Hcl, HOAc, and PO_4 buffers, showed substantially different behaviour (Fig. 1b and supplementary Fig. S1). Only the pH 2.8 condition showed significant reduction of the Au salt, with most other solutions only appearing slightly pink or clear with visible aggregates. The pH 2.8 condition used the lowest concentration of phosphate ions, when combined with the low mineralisation seen using the PO_4 buffer, suggest that the presence of phosphate is detrimental to ability of peptide B3 to reduce the gold salt. It also demonstrates that the ions present in solution must be considered alongside the change in pH

in determining the reaction kinetics of this system. The TBS buffer (pH 7.4), used in previous studies [19,31], produced a purple solution by contrast with a broad-spectrum absorbance in the NIR region and a distinct shoulder in the spectrum at ~650 nm, indicating the formation of particles of more complex geometry.

The effect of the buffer concentration was further investigated using HCl-KCl buffer (pH 1.6) and TBS (pH 7.4), which revealed the potential for the formation of AuNPs exhibiting NIR absorbance. AuNP synthesis was conducted using various concentrations of TBS (0–50 mM, pH 7.4; Fig. 1c) and HCl-KCl (25–200 mM, pH 1.6; Fig. 1d) at fixed concentrations of $HAuCl_4$ (0.5 mM) and the B3 peptide (0.25 mM). At higher buffer concentrations, no mineralisation was observed; specifically, at greater than 25 mM TBS and 175 mM HCl-KCl buffer, there was no obvious absorbance noted. On the contrary, at lower concentrations, distinct absorbance peaks were observed, indicating AuNP formation. Interestingly, the buffer concentrations affected the peaks in the NIR region (Fig. 1c-d and Supplementary Fig. S2). These results suggested that fine-tuning the pH and buffer concentration could provide a possible method to confer NIR absorbance to AuNPs. However, a major concern about working with peptides at pH 1.6 is the hydrolytic cleavage of amide bonds at low pH [39,40]. Since TBS (pH 7.4) offered significantly milder chemical conditions than HCl-KCl buffer (pH 1.6), the TBS-based condition was investigated in the subsequent analyses.

3.2. Dependency of AuNP biomineralisation on the B3 peptide concentration

The effects of peptide concentration on the optical properties of the mineralized AuNPs were investigated by varying the concentration of the B3 peptide from 0.1 to 1 mM. At concentrations above 0.5 mM, a single distinct peak at approximately 540 nm was observed (Fig. 2a). However, at concentrations lower than 0.5 mM, in addition to the first peak at 540 nm, a second peak was observed in the NIR region, which gradually red-shifted with decreasing B3 peptide concentration. The peptide concentration dependency of this second peak is displayed in Fig. 2b. The morphology of the synthesised AuNPs with different peptide concentrations (0.14, 0.18, 0.22, 0.26, and 0.30 mM) was observed by

TEM (Fig. 2c and supplementary Fig. S3). All the samples comprised two distinct populations of particle morphologies: decahedral AuNPs and TrAuNPls. As summarised in Table 2, the proportion of TrAuNPls (%TrAuNPls/AuNPs) was maximised at 0.18 mM peptide concentration (24.0%). The sizes of both the TrAuNPls and decahedral AuNPs were greatest at 0.18 mM and decreased in size with increasing peptide concentration above this (Table 2 and Supplementary Fig. S3). Decreasing the peptide concentration to 0.14 mM also resulted in a decrease in size. This was likely because there was insufficient peptide molecules to completely reduce tall of the gold ions in the solution. Interestingly, particles synthesised with the peptide at 0.12 mM displayed irregular wave edge structures along their edges compared with those synthesised using other peptide concentrations (Supplementary Fig. S4). Since the LSPR peaks of AuNPls are highly dependent on the particle size and morphology in comparison with decahedral AuNPs [38,39], a redshift of the red/NIR extinction peak is expected with increasing TrAuNPl edge length (which is supported by simulated optical properties of the AuNPs (Supplementary Figs. S5-7). The synthesised AuNPs show good stability over a period of 50 days, maintaining characteristic extinction spectra when stored at 4°C, implying that the AuNPs were stably dispersed over this timescale (Supplementary Fig. S8).

3.3. Characterisation of the B3 peptide using amino acid substitution derivatives

To specify the key amino acid for controlled AuNP mineralisation, B3 derivatives were designed with a single amino acid substitution (Fig. 3). In the B3 sequence ASHQWAWKWE, histidine (H), lysine (K), and glutamic acid (E) were substituted with alanine (A). The UV-visible spectrum of the particles synthesised using B3_E10A (the 10^{th} amino acid, E, was replaced with A) showed no significant difference compared with that of particles synthesised using the original B3 peptide (Fig. 3a, left panel). However, the B3_K8A sample (the eighth amino acid, K, was replaced with A) revealed aggregation of the synthesised AuNPs (Fig. 3a), while the B3_H3A sample (the third amino acid, H, replaced with A) clearly showed the different red/NIR peaks at about 650 nm compared with that produced by the original B3 peptide at approximately 700 nm. This suggests that H (potentially alongside K) in B3 plays a key

role in the morphological and/or size regulation of the synthesised AuNPs.

To gain further insight, the third amino acid H was further replaced with other characteristic amino acids, including E (acidic), W (tryptophan, aromatic), and K (anionic). Interestingly, AuNPs synthesised with these peptides (original B3, B3_H3A, B3_H3E, B3_H3W, and B3_H3K) showed UV-visible spectra containing various peaks in the NIR (Fig. 3a, right panel). Surprisingly, B3_H3A and B3_H3E synthesised AuNPls with circular morphology, while the other two peptides synthesised TrAuNPls (Fig. 3b), similar to those by the original B3 peptide. Based on the TEM-based imaging analysis of more than 200 randomly selected AuNPls, the size and circularity were quantified (Table 3) and various sizes of AuNPls from 25.1 (H3E) to 41.2 nm (B3) were observed using these peptides. AuNPls produced with B3, B3_H3W, and B3_H3K exhibited similar circularity (approximately 0.82), and those with B3_H3A and B3_H3E had a higher circularity (0.86 and 0.88, respectively). Both high-resolution TEM and fast Fourier transform patterns confirmed the single-crystalline nature of AuNPls (Fig. 3c). Such rounded particles will have blue-shifted LSPR peaks compared to the sharp-cornered angular plates seen under other conditions (Supplementary Fig. S6c). Simulated spectra were consistent with the blue-shifted higher wavelength peaks seen in the UV-visible spectra obtained of AuNPls synthesized using B3_H3A and B3_H3E. These findings indicate the importance of the third amino acid, H, in the B3 peptide in regulating morphology during Au mineralisation.

3.4. Scanning electron microscopy and XPS surface analysis of the AuNPls biomineralised with the B3 peptide

AuNPls synthesised using the original B3 peptide (0.25 mM peptide and 0.5 mM $HAuCl_4$) were observed by scanning electron microscopy (SEM) and analysed by XPS to understand the surface attachment of the peptide to AuNPls post-synthesis (Fig. 4). AuNPls and particles washed with 0.1 M Hypochlorous acid to remove organic molecules from the surface were observed by SEM. An organic layer was observed on both decahedral AuNPs and TrAuNPls post-synthesis; however, this layer was not observed after washing (Fig. 4a). This indicated that a peptide layer was present in all the observed

particle morphologies.

The XPS survey scan predominantly showed peaks for Au and N, as well as the predominant peak associated with the Indium (In) substrate (Fig. 4b). The relatively low Au signal was due to the low quantity of AuNPls transferred onto the substrate. The Au peaks of the spin-orbital doublet, Au $4f_{7/2,}$ and Au $4f_{5/2}$, were detected at binding energies (BEs) of 83.1 eV and 86.8 eV, respectively, and were consistent with the presence of Au^0. The BE of the Au $4f_{5/2}$ peak of bulk Au is 83.9 eV, which is significantly higher than that of the AuNPs (83.1 eV) synthesised with the B3 peptide. Such chemical shifts are generally caused by the surface chemistry and size of the particles. C and O were also detected; however, these were present on the In substrate with abundances similar to that of the AuNPs, and as such, it is not possible to separate signals associated with the peptide and contaminants already present on the surface. Detailed fitting of the C 1s peak revealed a peak at 286.2 eV, which was not found on the In substrate. This BE position is likely to be associated with the C-O groups of the B3 peptide. N was also detected in the AuNP sample, while it was not present in the In substrate reference sample. The N 1s peak was found at 398.8 eV and was associated with the presence of the B3 peptide. XPS is surface sensitive and tends to inflate the immediate surface composition compared with the entire nanoparticle composition. These results using SEM and XPS successfully showed the presence of peptide layers over the synthesised AuNPs, which might contribute to controlling the morphology of AuNPs.

3.5. Biocompatibility evaluation of AuNPs synthesised by B3 peptide

In order to investigate the cytotoxicity of synthesized AuNPs by B3 peptide (B3-AuNPs), the compatibility was assessed in Normal Human Dermal Fibroblast (NHDF) cell line and compared that with cetyltrimethylammonium chloride (CTAC)-capped Au nanorods (Fig. 5). The representative bright field image showed that the cells are spindle-shaped even in the presence of B3-AuNPs at 80 μg/mL, while the cells were spherically-shaped in the presence of CTAC-capped Au nanorod (CTAC-AuNRs) at 10 μg/mL (Fig. 5a). As the cell in the absence of any AuNPs were spindle-shaped the CTAC-capped AuNRs seem to have caused toxicity to the cells. In the observation of co-stained cells by calcein-AM

(green, live cell) and PI (red, dead cell), there was no decrease in viability in the NHDF cells exposed to peptide-synthesized AuNPs up to concentrations of 80 µg/mL, indicating the high biocompatibility. In contrast, the viability of NHDF cells dropped significantly with increasing CTAC-AuNR concentration, from (55 ± 5) (55 ± 5) % at 5 ug mL^{-1} and to (1 ± 1)% at 10 µg/mL, consistent with an IC_{50} of (5.4 +/- 0.3) µg/mL, which is presumably due to the toxicity from CTAC molecules capping on Au nanorods (Fig. 5b).

3.6. Photothermal activity of the biomineralised AuNPs

The photothermal conversion efficiency of these particles was measured *in vitro* by observing the increase in temperature under laser illumination (Fig. 6a). AuNP samples prepared using peptides having concentrations of 0.16, 0.20, 0.24, and 0.28 mM showed temperature increases of approximately 6 °C (22 to 28 °C) over 10 min of irradiation, while no significant temperature increase was found for the AuNPs synthesised without the peptide and those with 0.12 mM peptide (Fig. 6b). A temperature increase of 6 °C corresponds to a lower limit of photothermal efficiency of ~40% (Fig. S9), however this value is likely higher due to it being impossible to eliminate thermal losses from this calculation. In addition, as a control AuNPs, 4 nm in size, with absorbance at 525 nm (2.10 nM) were measured and exhibited very weak photothermal activity. The photothermal activity of the B3-AuNPs was further evaluated in cultured cancer cells. The cells were incubated at 37 °C with AuNPs prepared using 0.25 mM peptide and photoirradiated with a xenon lamp. After irradiation, cell viability was assessed using a live/dead cell assay, where calcein-AM and propidium iodide indicated live (green fluorescence) and dead cells (red fluorescence), respectively (Fig. 6c). Compared with the control, in which the same volume of PBS was added to the culture medium, AuNPs synthesised using the B3 peptide efficiently killed cancer cells by the photothermal effect under NIR light irradiation, indicating the potential use of AuNPs synthesised using B3 peptide in photothermal therapy by NIR light irradiation.

4. Discussion

This study investigated the conditions for the mineralisation of TrAuNPls using the B3 peptide (ASHQWAWKWE) in a simple green one-pot synthetic process. The mineralisation proceeded under ambient conditions by mixing only the peptide and Au(III) ions in an aqueous solution at 25 °C. Only a few studies on AuNP mineralisation peptides similar to the B3 peptide have been conducted. The GBP1 (MHGKTQATSGTIQS) peptide and some candidate sequences were originally isolated as metallic AuNP binding peptides from an *Escherichia coli* cell surface display library [43]. Subsequently, AuNP mineralisation using these peptides has been shown to result in a non-uniform morphology, which includes platelet structures [44,45]. The A3 peptide (AYSSGAPPMPPF) was isolated from a phage display library. This peptide and its derivatives mineralise spherical AuNPs of approximately 10 nm in size in HEPES buffer at pH 7.2 [33,46]. The Midas-2 (TGTSVLIATPYV) peptide yields polydisperse spherical AuNPs at pH 7.5 in PBS [32], while the Midas-2 mutant, Midas-11 (TGTSVLIATPGV), biomineralises AuNPs with various morphologies, including large AuNPls as wide as 125 µm with hexagonal and triangular shapes, depending on the pH of the reaction solution and Au ion and peptide concentrations [47].

In this study, using the B3 peptide, AuNP mineralisation was first investigated in different buffers at varying pH to effectively obtain AuNPs with a strong NIR absorbance (Figs. 1 and 2). We found a low pH, rather than the differences in the utilised buffers, to have a high impact on the optical properties of the AuNPs produced. This observation was comparable with a study on the Midas-11 peptide, which showed that AuNPls are effectively synthesised at pH 3.0 or lower [47]. However, as the UV-visible spectrum of Midas-11 shows a broad range of absorption over 500 nm, the solution seems to contain particles with a wide range of shapes. In contrast, the B3-based AuNP solution mainly showed two clear LSPR extinction peaks at approximately 540 nm (the first peak) and over 600 nm (the second peak). Finite Element Method (FEM) simulations showed that this lower peak was likely associated with smaller decahedra (Supplementary Fig. S5) and the peak in the red/NIR was associated with the synthesised plates (Supplementary Fig. S6 and 7). These simulations also showed that the NIR extinction peak was predominantly absorbance, making them suitable for use as photothermal conversion agents in

the NIR. Surprisingly, the presence of the second peak was noted even at the neutral pH 7.4 (TBS), which implies the development of a technique for producing AuNPs with NIR absorbance under mild conditions. For further characterisation, the effects of different buffer concentrations were investigated using TBS (pH 7.4) and HCl-KCl (pH 1.6). With increasing buffer concentration, the second peak was found to gradually redshift (Fig. 1 and Supplementary Fig. S2), and both peaks disappeared at high buffer concentrations. Suggesting that weaker mineralisation reaction conditions can effectively yield AuNPs with NIR absorbance. This is probably because weaker mineralisation conditions resulted in multiple mineralisation reactions on the immature particles, which enabled the formation of larger AuNPs.

Furthermore, the peptide concentration dependency was investigated by UV-visible spectroscopy and TEM (Table 2 and Supplementary Fig. S3). Lower peptide concentrations resulted in larger TrAuNPls with increasing absorbance at higher wavelengths. At 0.10 mM, only a single peak at 540 nm was observed. At higher peptide concentrations, faceted AuNPs were produced, and as the peptide concentration was reduced to ~0.12 mM, the external facets of the NPs became less crystalline with visible irregular terracing (arrows in Supplementary Fig. S4). This likely results from patchy capping by the peptide at these low concentrations, resulting in poorly regulated particle growth on all facets. It is notable that in both of the crystal morphologies discussed here, the major facets were {111} (with the edge facets of the plates alternating between {100} and {110}). The formation of particles of different shapes during synthesis is typically described in terms of minimising the Gibbs free surface energy, which results in the preferential expression of specific crystal facets [48]. In face-centred cubic noble metals (e.g., Au and Ag), the surface Gibbs free energies usually increase in the order of $a_{(111)} < a_{(100)} < a_{(110)}$ [49,50]. This typically results in the synthesis of populations of single-crystalline particles described by Wulff constructions, such as octahedra and cubes, with the need for facet-specific capping agents to produce more complex shapes. In addition, multi-crystalline morphologies exist, such as decahedra, which feature several {111} facets at a cost of having internal twinned defects. Hence, the observation of large populations of decahedra and nanoplates is highly indicative of this peptide being capable of

binding to {111} facets. Indeed, the only real distinction between these two morphologies with regards to synthesis is whether the nascent 'seed' particles from which they grow are multiply twinned or single crystalline. This is a highly desirable trait because if combined with nucleation control, it offers a potential strategy to produce such particles with a high shape yield.

At high B3 peptide concentrations, decahedral AuNPs predominantly expressing {111} facets were formed due to the fast biomineralisation reaction. With a decrease in the peptide concentration, during relatively slow biomineralisation events, TrAuNPls including {111}, {110}, and {100} facets were formed. At lower concentrations, larger AuNPls formed due to {111} surface capping, which prevented Au(III) ions from approaching the surface. Consequently, the growth of the particle was induced in the {110} and {100} directions to form a flat and wide {111} surface. At an even lower concentration (e.g., 0.12 mM), the absence of the B3 peptide at the {110} and {100} facets revealed the loss of uniform mineralisation with a wavy particle structure (Supplementary Fig. S4). The packing density of the peptide at each facet will also affect the morphology control. Although the presence of peptide molecules on the crystal surfaces was confirmed by SEM and XPS analyses in this study (Fig. 4), further investigations should be conducted to elucidate the mineralisation reaction.

In this study, adjusting the peptide concentration enabled tuning of the size and optical properties of the synthesised AuNPls. Furthermore, using B3 peptide derivatives, the morphology of AuNPls could be modified, for example, from triangular plates to discs (Fig. 3). In the previous reports on the crystallographic influence of proteins and peptides during crystal growth, the direct interactions with specific crystallographic faces and round edges have been observed [51–53]. Because of this interaction between the peptide and nanoparticles, the growth kinetics and thermodynamics change and can consequently alter the morphology of crystals. Using B3 derivatives, triangular plates and more circular plates were synthesized according to their sequence. This might be probably because the alteration of direct interaction manner between the AuNP surface and the third amino acid in B3 peptide (Fig. 7). On the other hand, organic homogeneous layer presumably consisting of peptides was clearly observed on the as-synthesised AuNPs (Fig. 4). The observation suggests that mineralisation peptide utilised in this

study self-assembles on AuNPs accompanying with the particle synthesis regulation. Therefore, the alteration of peptide structure due to the mutation of third amino acid in B3 may contribute for the morphological regulation (Fig. 7). To fully understand both interactions of particle-peptide and peptide-peptide, further studies that include crystallographic structural analysis, kinetic evaluation and molecular dynamic simulation are required.

AuNPl synthesis occurred by mixing the peptide and metallic ions in the buffer solution at neutral pH. Compared with conventional methods, this protocol is much more eco-friendly. Furthermore, the morphological control offered by this peptide enabling the synthesis of TrAuNPls has great potential in a wide range of applications, such as biosensing, cell imaging, and optical coating for solar energy converters. Concerns for the environmental impact on the use of organic solvents in some of AuNPls syntheses and use of the synthesised nanomaterials in biological applications have motivated the search for more environmentally benign alternatives to chemical synthesis [12–14]. In this study, TrAuNPls synthesis via a one-pot process of mixing $HAuCl_4$ and peptides at room temperature were investigated. To investigate the cytotoxicity of synthesized AuNPs containing TrAuNPls, the compatibility was assessed in NHDF cells and compared that with CTAC-capped Au nanorods (Fig. 5). As the higher biocompatibility of AuNPs synthesised with B3 peptide in comparison with CTAC-capped Au nanorods was found, the photothermal effect of AuNPs without any washing or purification processes was conducted and confirmed the potential usage for cancer therapy (Fig. 6). As these data clearly disclose the potential of AuNPs synthesised by peptide especially for biomedical fields, further investigations will be conducted such as *in vivo* experiments.

The yield of TrAuNPls was maximised to 24% with 0.18 mM B3 peptide in TBS buffer (pH 7.4). In this condition, the size range of synthesised TrAuNPls was 67 ± 27 nm. The low yield and large size distribution compared with other synthesis protocol including CTAC-based techniques are still problematic for the applications. As various techniques such as sucrose density gradient centrifugation, electrophoresis and flocculation were trialed in previous literatures [54–56], the technique development of TrAuNPls synthesised by peptide will be conducted in the future. Herein, decahedra and pentatwinned

particles were observed and the surfaces of these morphologies are dominated by {111} facets. This is strongly suggestive that the B3 peptide has the ability to stabilise {111} facets. The final morphology of the particles will be dictated by the nascent 'seed' particles which are initially nucleated by the peptide, with pentatwinned seeds leading to decahedra and single crystalline seeds leading to nanoplates. The control monocrystallinity of the initially nucleated particles by the peptide will make it possible to achieve higher yield. Further improvements in the desired morphology yield and purification process using these techniques would provide a significant benefit because the synthesis is a very simple, safe, and green process, not requiring any harsh chemicals such as organic solvents and surfactants.

5. Conclusions

In this study, we focused on the characterisation of TrAuNPls mineralised with the B3 peptide using a facile green one-step protocol performed under ambient conditions. The protocol consisted of simply mixing a pre-engineered peptide sequence with a gold salt in a buffer, with no additional need for reduction or capping agents. By analysing multiple reaction conditions, such as pH, buffer concentration, and the reacting peptide concentration, it was possible to synthesise TrAuNPls with adjustable NIR absorbance. The yield was maximised to 24% with 0.18 mM B3 peptide. Moreover, to the best of our knowledge, this is the first study to reveal the potential for controlled circular AuNPl synthesis using peptides. In addition, we demonstrated that B3-AuNPs could be used for cancer photothermal therapy *in vitro*. Our findings could contribute to the development of new techniques for size- and morphology-based controlled AuNPl synthesis using non-toxic molecules under mild conditions for biological applications.

Acknowledgements

This work was supported by a Grant-in-Aid for Scientific Research from the Ministry of Education, Sports, Science, and Technology, Japan [grant numbers 18H01795, 18K18970, 18K04848, 21H01726, 21H01725]; the International Collaboration Research Projects (the JSPS and the Royal Society) [grant

number IEC/R3/170038]; the Cross-Ministerial Strategic Innovation Promotion Program (SIP), the Cabinet Office, Government of Japan; the Iketani Science and Technology Foundation (to M.T.); the Murata Science Foundation (to M.T. and T.N.); the EPSRC (to K.C.) [grant numbers EP/P005233/1, EP/T013753/1]; and the Tokyo Tech Fund (Interdisciplinary Research Support for Scientists) (to M.T. and T.N.). L.R. would like to thank the University of Leeds for the award of a Ph.D. studentship through the University Research Scholarship. The authors thank Suzukakedai Materials Analysis Division, Technical Department, Tokyo Institute of Technology, for mass spectrometry analysis. In addition, the authors acknowledge the O-okayama Materials Analysis Division of Tokyo Institute of Technology for their assistance with the TEM and SEM analyses.

Disclosures

The authors declare that they have no known competing financial interests or personal relationships that could have appeared to influence the work reported in this paper.

References

[1] J. Liu, Q. Peng, Protein-gold nanoparticle interactions and their possible impact on biomedical applications, Acta Biomater. 55 (2017) 13–27. https://doi.org/10.1016/j.actbio.2017.03.055.

[2] R.S. Riley, E.S. Day, Gold nanoparticle-mediated photothermal therapy: Applications and opportunities for multimodal cancer treatment, Wiley Interdiscip. Rev. Nanomed. Nanobiotechnology 9 (2017). https://doi.org/10.1002/wnan.1449.

[3] S. Her, D.A. Jaffray, C. Allen, Gold nanoparticles for applications in cancer radiotherapy: Mechanisms and recent advancements, Adv. Drug Deliv. Rev. 109 (2017) 84–101. https://doi.org/10.1016/J.ADDR.2015.12.012.

[4] F. Gao, G. He, H. Yin, J. Chen, Y. Liu, C. Lan, S. Zhang, B. Yang, Titania-coated 2D gold nanoplates as nanoagents for synergistic photothermal/sonodynamic therapy in the second near-infrared window, Nanoscale 11 (2019) 2374–2384. https://doi.org/10.1039/c8nr07188h.

[5] L. Roach, S. Ye, S.C.T. Moorcroft, K. Critchley, P.L. Coletta, S.D. Evans, Morphological control of seedlessly-synthesized gold nanorods using binary surfactants, Nanotechnology 29 (2018) 135601. https://doi.org/10.1088/1361-6528/aaa99d.

[6] A.R. Rastinehad, H. Anastos, E. Wajswol, J.S. Winoker, J.P. Sfakianos, S.K. Doppalapudi, M.R. Carrick, C.J. Knauer, B. Taouli, S.C. Lewis, A.K. Tewari, J.A. Schwartz, S.E. Canfield, A.K. George, J.L. West, N.J. Halas, Gold nanoshell-localized photothermal ablation of prostate tumors in a clinical pilot device study, Proc. Natl. Acad. Sci. U. S. A. 116 (2019) 18590–18596. https://doi.org/10.1073/pnas.1906929116.

[7] L. Roach, M.E. Booth, N. Ingram, D.A. Peterson, D.V.B. Batchelor, S.C.T. Moorcroft, R.J. Bushby, K. Critchley, P.L. Coletta, S.D. Evans, Evaluating phospholipid-functionalized gold nanorods for *in vivo* applications. Small (2021) 2006797. https://doi.org/10.1002/smll.202006797

[8] A. Miranda, E. Malheiro, E. Skiba, P. Quaresma, P.A. Carvalho, P. Eaton, B. de Castro, J.A. Shelnutt, E. Pereira, One-pot synthesis of triangular gold nanoplates allowing broad and fine tuning of edge length, Nanoscale 2 (2010) 2209–2216. https://doi.org/10.1039/c0nr00337a.

[9] W. Ye, K. Krüger, A. Sánchez-Iglesias, I. García, X. Jia, J. Sutter, S. Celiksoy, B. Foerster, L.M. Liz-Marzán, R. Ahijado-Guzmán, C. Sönnichsen, CTAB stabilizes silver on gold nanorods, Chem. Mater. 32 (2020) 1650–1656. https://doi.org/10.1021/acs.chemmater.9b05139.

[10] D. Mirska, K. Schirmer, S.S. Funari, A. Langner, B. Dobner, G. Brezesinski, Biophysical and biochemical properties of a binary lipid mixture for DNA transfection, Colloids Surf. B Biointerfaces 40 (2005) 51–59. https://doi.org/10.1016/j.colsurfb.2004.10.007.

[11] D.K. Smith, B.A. Korgel, The importance of the CTAB surfactant on the colloidal seed-mediated synthesis of gold nanorods, Langmuir 24 (2008) 644–649. https://doi.org/10.1021/la703625a.

[12] Y. Tan, J. Lee, D. Wang, Aspartic acid synthesis of crystalline gold nanoplates, nanoribbons, and nanowires in aqueous solutions, J. Phys. Chem. C 112 (2008) 5463–5470. https://doi.org/10.1021/jp800501k

[13] Y. Chen, Z. Lee, M Li, Z Wu, J You, C Li, Guiding growth orientation of two-dimensional Au

nanocrystals with marine chitin nanofibrils for ultrasensitive and ultrafast sensing hybrids, J. Mater. Chem. B 5 (2017) 9502. https://doi.org/10.1039/C7TB02792C

[14] G. Wang, S. Tao, Y. Liu, L. Guo, V. Qin, K. Ijiro, M. Maeda, Y Yin, High-yield halide-free synthesis of biocompatible Au nanoplates, Chem. Commun. 52 (2016) 398–401. https://doi.org/10.1021/jp800501k

[15] S. Mann, Molecular tectonics in biomineralization and biomimetic materials chemistry, Nature 365 (1993) 499–505. https://doi.org/10.1038/365499a0.

[16] L.A. Estroff, Introduction: Biomineralization, Chem. Rev. 108 (2008) 4329–4331. https://doi.org/10.1021/cr8004789.

[17] L. Addadi, S. Weiner, Control and design principles in biological mineralization, Angew. Chem. Int. Ed. Engl. 31 (1992) 153–169. https://doi.org/10.1002/anie.199201531.

[18] N. Kasyanenko, M. Varshavskii, E. Ikonnikov, E. Tolstyko, R. Belykh, P. Sokolov, V. Bakulev, V. Rolich, K. Lopatko, DNA modified with metal nanoparticles: Preparation and characterization of ordered metal-DNA nanostructures in a solution and on a substrate, J. Nanomater. 2016 (2016) 1–12. https://doi.org/10.1155/2016/3237250, http://www.ncbi.nlm.nih.gov/pubmed/3237250.

[19] K. Zagorovsky, L.Y.T. Chou, W.C.W. Chan, Controlling DNA-nanoparticle serum interactions, Proc. Natl. Acad. Sci. U. S. A. 113 (2016) 13600–13605. https://doi.org/10.1073/pnas.1610028113.

[20] H. Li, L. Rothberg, Colorimetric detection of DNA sequences based on electrostatic interactions with unmodified gold nanoparticles, Proc. Natl. Acad. Sci. U. S. A. 101 (2004) 14036–14039. https://doi.org/10.1073/pnas.0406115101.

[21] T. Hatanaka, A. Matsugami, T. Nonaka, H. Takagi, F. Hayashi, T. Tani, N. Ishida, Rationally designed mineralization for selective recovery of the rare earth elements, Nat. Commun. 8 (2017) 15670. https://doi.org/10.1038/ncomms15670.

[22] M. Tanaka, Y. Takahashi, L. Roach, K. Critchley, S.D. Evans, M. Okochi, Rational screening of biomineralisation peptides for colour-selected one-pot gold nanoparticle syntheses, Nanoscale

Adv. 1 (2019) 71–75. https://doi.org/10.1039/C8NA00075A.

[23] Y. Maeda, O.V. Makhlynets, H. Matsui, I.V. Korendovych, Design of catalytic peptides and proteins through rational and combinatorial approaches, Annu. Rev. Biomed. Eng. 18 (2016) 311–328. https://doi.org/10.1146/annurev-bioeng-111215-024421.

[24] A. Vallee, V. Humblot, C.M. Pradier, Peptide interactions with metal and oxide surfaces, Acc. Chem. Res. 43 (2010) 1297–1306. https://doi.org/10.1021/ar100017n.

[25] Z. Tang, J.P. Palafox-Hernandez, W.C. Law, Z.E. Hughes, M.T. Swihart, P.N. Prasad, M.R. Knecht, T.R. Walsh, Biomolecular recognition principles for bionanocombinatorics: An integrated approach to elucidate enthalpic and entropic factors, A.C.S. Nano 7 (2013) 9632–9646. https://doi.org/10.1021/nn404427y.

[26] Z. Zhang, W. Zhu, T. Kodadek, Selection and application of peptide-binding peptides, Nat. Biotechnol. 18 (2000) 71–74. https://doi.org/10.1038/71951.

[27] W. Yang, W. Guo, J. Chang, B. Zhang, Protein/peptide-templated biomimetic synthesis of inorganic nanoparticles for biomedical applications, J. Mater. Chem. B 5 (2017) 401–417. https://doi.org/10.1039/c6tb02308h.

[28] M.B. Dickerson, K.H. Sandhage, R.R. Naik, Protein- and peptide-directed syntheses of inorganic materials, Chem. Rev. 108 (2008) 4935–4978. https://doi.org/10.1021/cr8002328.

[29] C.L. Chen, N.L. Rosi, Peptide-based methods for the preparation of nanostructured inorganic materials, Angew. Chem. Int. Ed. Engl. 49 (2010) 1924–1942. https://doi.org/10.1002/anie.200903572.

[30] C.Y. Chiu, Y. Li, L. Ruan, X. Ye, C.B. Murray, Y. Huang, Platinum nanocrystals selectively shaped using facet-specific peptide sequences, Nat. Chem. 3 (2011) 393–399. https://doi.org/10.1038/nchem.1025.

[31] M. Tanaka, E. Mazuyama, A. Arakaki, T. Matsunaga, MMS6 protein regulates crystal morphology during nano-sized magnetite biomineralization *in vivo*, J. Biol. Chem. 286 (2011) 6386–6392. https://doi.org/10.1074/jbc.M110.183434.

[32] J. Kim, Y. Rheem, B. Yoo, Y. Chong, K.N. Bozhilov, D. Kim, M.J. Sadowsky, H.G. Hur, N.V. Myung, Peptide-mediated shape- and size-tunable synthesis of gold nanostructures, Acta Biomater. 6 (2010) 2681–2689. https://doi.org/10.1016/j.actbio.2010.01.019.

[33] J.M. Slocik, M.O. Stone, R.R. Naik, Synthesis of gold nanoparticles using multifunctional peptides, Small 1 (2005) 1048–1052. https://doi.org/10.1002/smll.200500172.

[34] M. Tanaka, S. Hikiba, K. Yamashita, M. Muto, M. Okochi, Array-based functional peptide screening and characterization of gold nanoparticle synthesis, Acta Biomater. 1 (2017) 495–506. https://doi.org/10.1016/j.actbio.2016.11.037.

[35] M. Tanaka, T. Suwatthanarak, A. Arakaki, B.R.G. Johnson, S.D. Evans, M. Okochi, S.S. Staniland, T. Matsunaga, Enhanced tubulation of liposome containing cardiolipin by MamY protein from magnetotactic bacteria, Biotechnol. J. 13 (2018) e1800087. https://doi.org/10.1002/biot.201800087.

[36] M. Okochi, M. Muto, K. Yanai, M. Tanaka, T. Onodera, J. Wang, H. Ueda, K. Toko, Array-based rational design of short peptide probe-derived from an anti-TNT monoclonal antibody, A.C.S. Comb. Sci. 19 (2017) 625–632. https://doi.org/10.1021/acscombsci.7b00035.

[37] G. Gomori, [16] Preparation of buffers for use in enzyme studies, Methods Enzymol. 1 (1955) 138–146. https://doi.org/10.1016/0076-6879(55)01020-3.

[38] P.B. Johonson, R.W. Christy, Optical constants of the noble metals, Phys. Rev. B 6, (1972) 4370–4379. https://doi.org/10.1103/PhysRevB.6.4370

[39] R.M. Smith, D.E. Hansen, The pH-rate profile for the hydrolysis of a peptide bond, J. Am. Chem. Soc. 120 (1998) 8910–8913. https://doi.org/10.1021/ja9804565.

[40] Y. Sun, M. Frenkel-Pinter, C.L. Liotta, M.A. Grover, The pH dependent mechanisms of non-enzymatic peptide bond cleavage reactions, Phys. Chem. Chem. Phys. 22 (2019) 107–113. https://doi.org/10.1039/c9cp05240b.

[41] J. Xie, J.Y. Lee, D.I.C. Wang, Y.P. Ting, Identification of active biomolecules in the high-yield synthesis of single-crystalline gold nanoplates in algal solutions, Small 3 (2007) 672–682.

https://doi.org/10.1002/smll.200600612.

[42] Y. Ni, C. Kan, J. Xu, Y. Liu, The synthesis of high yield Au nanoplate and optimized optical properties, Superlattices Microstruct. 114 (2018) 124–142. https://doi.org/10.1016/J.SPMI.2017.12.021.

[43] S. Brown, Metal-recognition by repeating polypeptides, Nat. Biotechnol. 15 (1997) 269–272. https://doi.org/10.1038/nbt0397-269.

[44] S. Brown, M. Sarikaya, E. Johnson, A genetic analysis of crystal growth, J. Mol. Biol. 299 (2000) 725–735. https://doi.org/10.1006/jmbi.2000.3682.

[45] Z. Wang, J. Chen, P. Yang, W. Yang, Biomimetic synthesis of gold nanoparticles and their aggregates using a polypeptide sequence, Appl. Organometal. Chem. 21 (2007) 645–651. https://doi.org/10.1002/aoc.1222.

[46] M.M. Tomczak, J.M. Slocik, M.O. Stone, R.R. Naik, Bio-based approaches to inorganic material synthesis, Biochem. Soc. Trans. 35 (2007) 512–515. https://doi.org/10.1042/BST0350512.

[47] J. Kim, D.H. Kim, S.J. Lee, Y. Rheem, N.V. Myung, H.G. Hur, Synthesis of gold structures by gold-binding peptide governed by concentration of gold ion and peptide, Biosci. Biotechnol. Biochem. 80 (2016) 1478–1483. https://doi.org/10.1080/09168451.2016.1176516.

[48] A. Abedini, A.A.A. Bakar, F. Larki, P.S. Menon, M.S. Islam, S. Shaari, Recent advances in shape-controlled synthesis of noble metal nanoparticles by radiolysis route, Nanoscale Res. Lett. 11 (2016) 287. https://doi.org/10.1186/s11671-016-1500-z.

[49] J.M. Zhang, F. Ma, K.W. Xu, Calculation of the surface energy of FCC metals with modified embedded-atom method, Appl. Surf. Sci. 229 (2004) 34–42. https://doi.org/10.1016/j.apsusc.2003.09.050.

[50] Y. Xiong, B.J. Wiley, Y. Xia, Nanocrystals with unconventional shapes – A class of promising catalysts, Angew. Chem. Int. Ed. Engl. 46 (2007) 7157–7159. https://doi.org/10.1002/anie.200702473.

[51] H.H. Teng, P.M. Dove, C.A. Orme, J.J. De Yoreo, Thermodynamics of calcite growth: baseline

for understanding biomineral formation, Science 282 (1998) 724–727. https://doi.org/10.1126/science.282.5389.724

[52] J.J. De Yoreo, A. Wierzbicki, P.M. Dove, New insights into mechanisms of biomolecular control on growth of inorganic crystals, Cryst. Eng. Comm. 9 (2007) 1144–1152. https://doi.org/10.1039/b713006f

[53] A. Yamagishi, K. Narumiya, M. Tanaka, T. Matsunaga, A. Arakaki, Core amino acid residues in the morphology-regulating protein, Mms6, for intracellular magnetite biomineralization, Sci. Rep. 6 (2016) 1–10. https://doi.org/10.1038/srep35670

[54] W. Wu, J. Huang, L. Wu, D. Sun, L. Lin, Y. Zhou, H. Wang, Q. Li, Two-step size- and shape-separation of biosynthesized gold nanoparticles, Sep. Purif. Technol. 106 (2013) 117–122. https://doi.org/10.1016/j.seppur.2013.01.005

[55] X. Xu, K.K. Caswell, E. Thcker, S. Kabisatpathy, K.L. Brodhacker, W.A. Scrivens, Size and shape separation of gold nanoparticles with preparative gel electrophoresis, J. Chromatogr. A. 1167 (2007) 35–41. https://doi.org/10.1016/j.chroma.2007.07.056

[56] L. Scarabelli, M. Coronado-Puchau, J.J. Giner-Casares, J. Langer, L.M. Liz-Marzán, Size and shape separation of gold nanoparticles with preparative gel electrophoresis, J. Chromatogr. A. 1167 (2007) 35–41. https://doi.org/10.1016/j.chroma.2007.07.056

Figure legends

Table 1 A list of the different buffers used for attaining pH control.

Table 2 Table 2. The size and yield distributions of Au nanoparticles synthesised using different concentrations of the B3 peptide.

Table 3. Circularity of triangular Au nanoplates synthesised using B3 peptide derivatives.

Fig. 1 Synthesis of Au nanoparticles using the B3 peptide in different buffers and pH conditions.

a) Microtiter plate showing the colour intensity produced for the synthesised Au nanoparticles (AuNPs) in the presence of the B3 peptide (0.25 mM) and $HAuCl_4$ (0.5 mM) after 24 h of mineralisation reaction in different buffers and pH conditions. b) UV-visible extinction spectra of peptide-synthesised AuNPs in different buffer. c) Evaluation of the effects of different TBS concentrations at pH 7.4 on AuNP mineralisation with the B3 peptide. d) Evaluation of the effects of different HCl-KCl buffer concentrations at pH 1.6 on AuNP mineralisation with the B3 peptide. The reactions in c) and d) were performed at fixed concentrations of the peptide (0.25 mM) and $HAuCl_4$ (0.5 mM). TBS, Tris-buffered saline.

Fig. 2 Synthesis of Au nanoparticles with different concentrations of the B3 peptide.

a) UV-visible extinction spectrum of each reaction solution containing Au nanoparticles (AuNPs) synthesised with different concentrations of the B3 peptide (0, 0.10-0.30, 0.50, and 1.00 mM). The reactions were performed at fixed concentrations of Tris-buffered saline (7 mM, pH 7.4) and $HAuCl_4$ (0.5 mM). b) Evaluation of the shift in the second peak with varying peptide concentrations. A gradual increase in wavelength is observed with decreasing B3 peptide concentration. c) Representative transmission electron microscopy (TEM) images of AuNPs produced in the presence of different concentrations of the B3 peptide (0.14, 0.18, 0.22, 0.26, and 0.30 mM) are shown. The scale bar indicates

200 nm.

Fig. 3 Synthesis of Au nanoparticles using B3 peptide derivatives.

a) UV-visible extinction spectrum of each reaction solution containing Au nanoparticles (AuNPs) synthesized with B3 peptide derivatives (0.25 mM). b) Representative transmission electron microscopy (TEM) images of AuNPs produced in the presence of different B3 peptide derivatives. The scale bar indicates 100 nm. c) High-resolution TEM images of Au nanoplates (AuNPls) with varying circularity mineralised by the original B3, B3_H3A, and B3_H3E peptides. The insets of the high-resolution TEM images depict the fast Fourier transform patterns.

Fig. 4 Surface analysis of Au nanoparticles synthesised using the B3 peptide with scanning electron microscopy and X-ray photoelectron spectroscopy.

a) Representative scanning electron microscopy (SEM) images of the decahedral Au nanoparticles (AuNPs) (left) and triangular Au nanoplates (right). The upper panel images are directly taken from the AuNPs synthesised using the B3 peptide, while the lower panel images are taken from particles after being subjected to treatment with hypochlorous acid in order to remove organic molecules on these crystals. The scale bar indicates 25 nm. b) X-ray photoelectron spectroscopy (XPS) analysis of AuNPs synthesised using the B3 peptide. A wide scan and detailed scans of each major region (C 1s, N 1s, and Au 4f) are shown. The dotted and solid lines are the (Shirley) background and peak components, respectively, while the dashed line is the summation of each peak fit and the background.

Fig. 5 Effects of B3-AuNPs on the cell viability and cytotoxicity in Normal Human Dermal Fibroblast (NHDF) cell line.

a) Representative bright field and fluorescent images of NHDF which are co-stained with calcein-AM (green) and PI (red) after 0, B3-AuNPs (10 μg/ml), B3-AuNPs (80 μg/ml) and Au nanorod cupped with cetyltrimethylammonium chloride, CTAC (10 μg/ml) exposure for 24 hours. Scale bar shows 100 μm. b)

Cell viability was assessed with increasing concentration of B3-AuNPs and CTAC-Au nanorod by manual count of more than 1,000 cells in total in the five fluorescent images. Values were represented as the percentages of cell viability compared with the number of inoculated cells. Error bars were defined as standard deviation (n=5).

Fig. 6 Evaluation of the photothermal activity of Au nanoparticles synthesised using the B3 peptide. a) The apparatus used for evaluating the photothermal effect. b) The reaction solution containing Au nanoparticles (AuNPs) synthesised using the B3 peptide at different concentrations (0.12–0.24 mM) was directly irradiated (>610 nm wavelength) and monitored with a thermometer probe. The 4 nm AuNPs with absorbance peak at 50 nm is synthesised by the conventional method using $NaBH_4$ as a reducing agent [30]. All syntheses were conducted with a constant concentration of Tris-buffered saline (7 mM) and $HAuCl_4$ (0.5 mM). c) Fluorescence images depicting the phototherapeutic effect of AuNPs synthesised using the B3 peptide (0.25 mM), as assessed by the cell viability assay. Red emission: dead cells and green emission: live cells. Ext., extinction; NP, nanoparticle; AuNP, Au nanoparticle; NIR, near-infrared.

Fig. 7 Proposed models for AuNPls morphological regulation by B3 derivatives.

Through the modification of third amino acid (H) in B3, the morphology of TrAuNPls was changed. From this observation, two possible mechanisms are considered; one is peptide-particle interaction and the other is peptide-peptide interaction.

Tables

Table 1. A list of the different buffers used for attaining pH control.

pH range	Buffer			
1.0–2.2	**HCl-KCl**	HCl/KCl		
2.8–3.4	**Gly-HCl**	HCl/glycine	**Cit-PO_4**	Citrate / phosphate
4.0–5.2	**HOAc**	Acetic acid/sodium acetate		
5.8–7.0	**PO_4**	Monobasic/dibasic phosphate		
7.4	**TBS**	Tris-buffered saline		

Table 2. The size and yield distributions of Au nanoparticles synthesised using different concentrations of the B3 peptide.

Peptide concentration (mM)		0.14	0.18	0.22	0.26	0.30
Feret diameter (nm)	AuNPs	32 ± 13	41 ± 7	32 ± 6	29 ± 6	24 ± 4
	TrAuNPls	60 ± 42 (22%)*	67 ± 27 (24%)	52 ± 21 (21%)	46 ± 17 (17%)	37 ± 12 (12%)

*The proportion of TrAuNPls in the solution is shown. AuNP, Au nanoparticle; TrAuNPl, triangular Au nanoplate.

Table 3. Circularity of triangular Au nanoplates synthesised using B3 peptide derivatives.

Peptides*	ASWQWAWKWE (H3W)	ASKQWAWKWE (H3K)	ASHQWAWKWE (B3)	ASAQWAWKWE (H3A)	ASEQWAWKWE (H3E)
Circularity	0.82 ± 0.05	0.82 ± 0.05	0.83 ± 0.05	0.86 ± 0.04	0.88 ± 0.03
Feret diameter (nm)	39 ± 15	34 ± 15	41 ± 15	30 ± 7	25 ± 6

*The amino acid substituted in the original B3 peptide is underlined.

Figure(s)

Click here to access/download;Figure(s);Tanaka.et.al.Figures.pptx

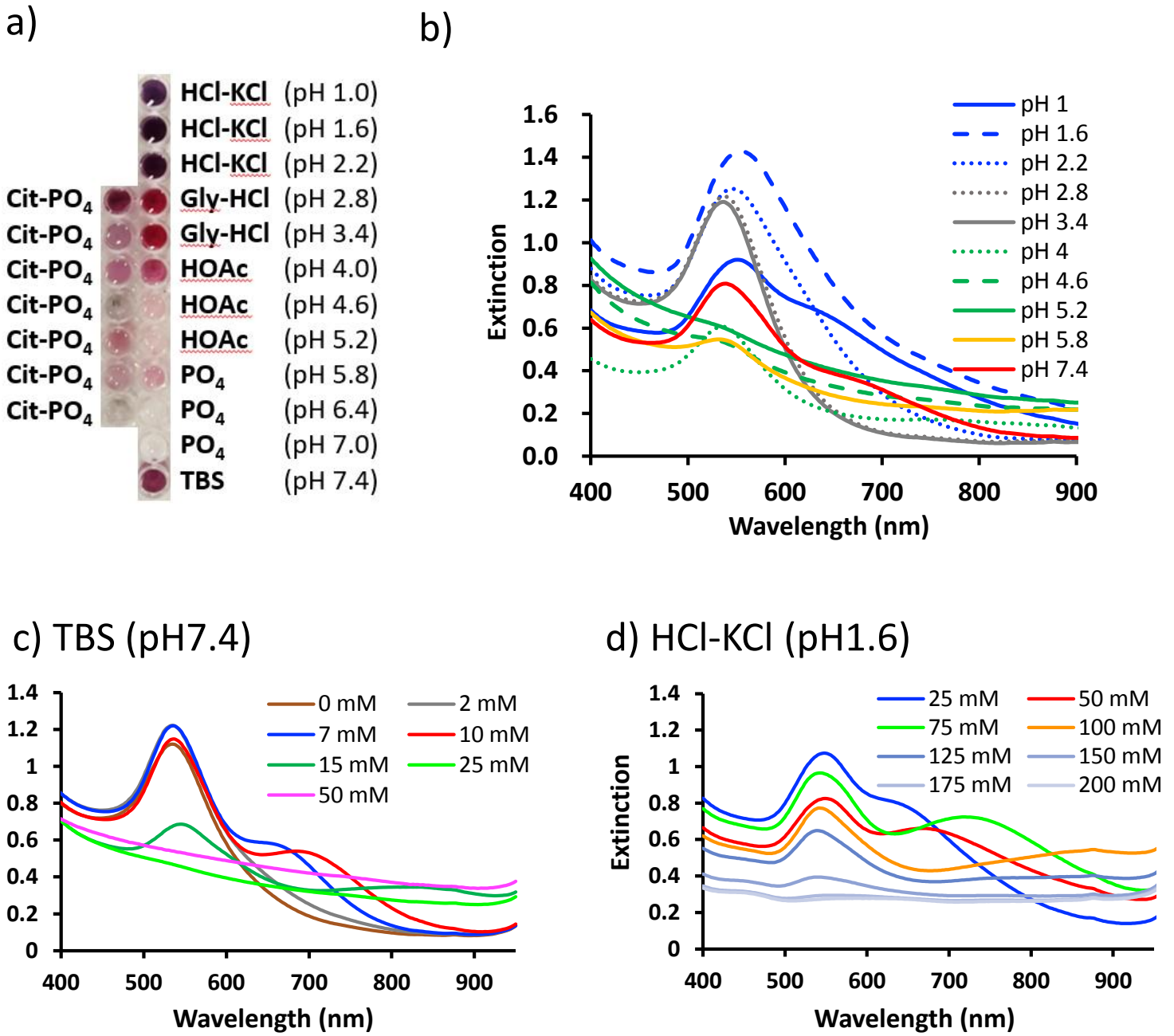

Fig. 1 Synthesis of Au nanoparticles using the B3 peptide in different buffers and pH conditions.

a) Microtiter plate showing the colour intensity produced for the synthesised Au nanoparticles (AuNPs) in the presence of the B3 peptide (0.25 mM) and $HAuCl_4$ (0.5 mM) after 24 h of mineralisation reaction in different buffers and pH conditions. b) UV-visible extinction spectrum of each reaction solution. c) Evaluation of the effects of different TBS concentrations at pH 7.4 on AuNP mineralisation with the B3 peptide. d) Evaluation of the effects of different HCl-KCl buffer concentrations at pH 1.6 on AuNP mineralisation with the B3 peptide. The reactions in c) and d) were performed at fixed concentrations of the peptide (0.25 mM) and $HAuCl_4$ (0.5 mM). TBS, Tris-buffered saline.

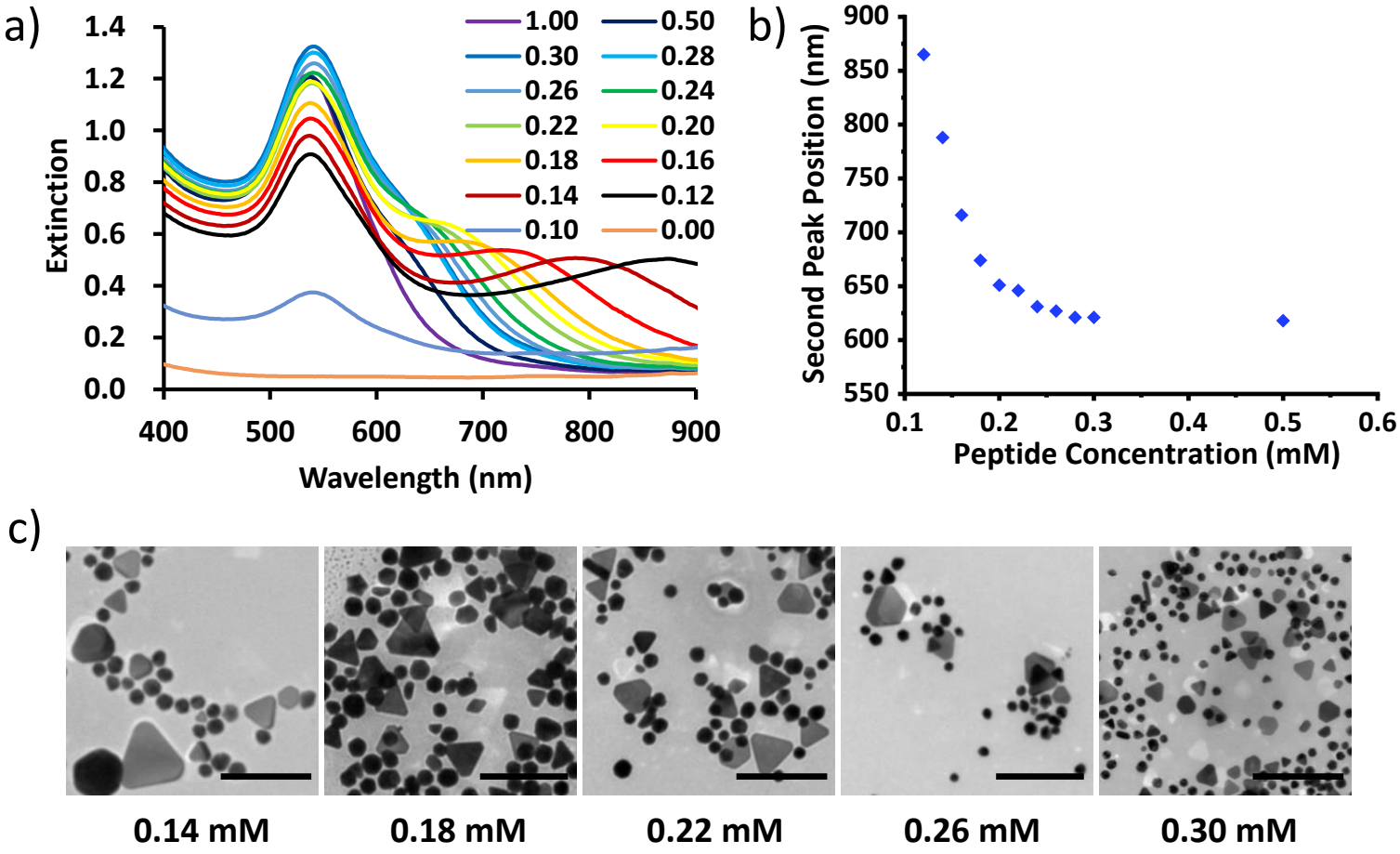

Fig. 2 Synthesis of Au nanoparticles with different concentrations of the B3 peptide.

a) UV-visible extinction spectrum of each reaction solution containing Au nanoparticles (AuNPs) synthesized with different concentrations of the B3 peptide (0, 0.10-0.30, 0.50, and 1.00 mM). The reactions were performed at fixed concentrations of Tris-buffered saline (7 mM, pH 7.4) and $HAuCl_4$ (0.5 mM). b) Evaluation of the shift in the second peak with varying peptide concentrations. A gradual increase in wavelength is observed with decreasing B3 peptide concentration. c) Representative transmission electron microscopy (TEM) images of AuNPs produced in the presence of different concentrations of the B3 peptide (0.14, 0.18, 0.22, 0.26, and 0.30 mM) are shown. The scale bar indicates 200 nm.

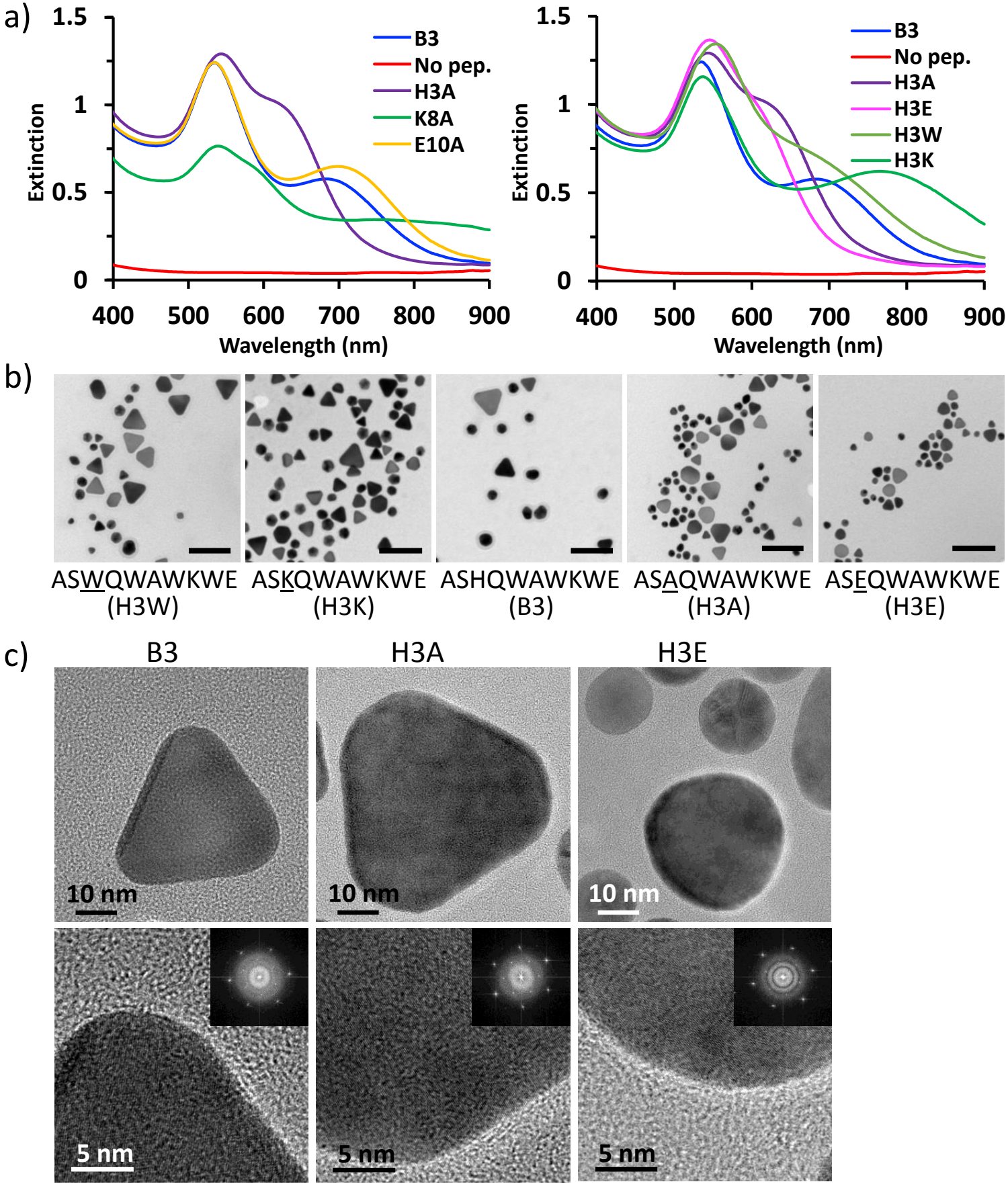

Fig. 3 Synthesis of Au nanoparticles using B3 peptide derivatives.

a) UV-visible extinction spectrum of each reaction solution containing Au nanoparticles (AuNPs) synthesized with B3 peptide derivatives (0.25 mM). b) Representative transmission electron microscopy (TEM) images of AuNPs produced in the presence of different B3 peptide derivatives. The scale bar indicates 100 nm. c) High-resolution TEM images of Au nanoplates (AuNPls) with varying circularity mineralised by the original B3, B3_H3A, and B3_H3E peptides. The insets of the high-resolution TEM images depict the fast Fourier transform patterns.

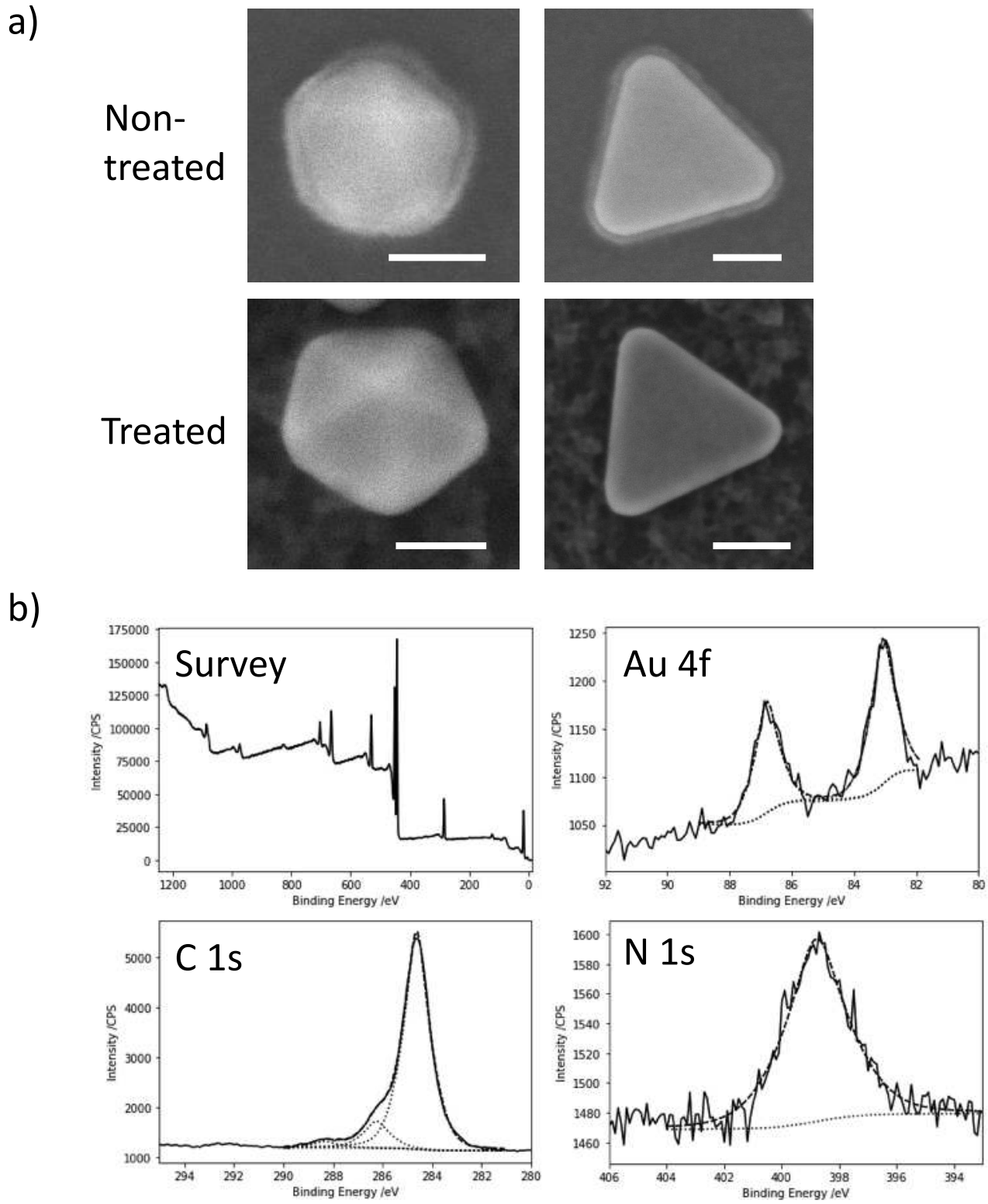

Fig. 4 Surface analysis of Au nanoparticles synthesised using the B3 peptide with scanning electron microscopy and X-ray photoelectron spectroscopy.

a) Representative scanning electron microscopy (SEM) images of the decahedral Au nanoparticles (AuNPs) (left) and triangular Au nanoplates (right). The upper panel images are directly taken from the AuNPs synthesised using the B3 peptide, while the lower panel images are taken from particles after being subjected to treatment with hypochlorous acid in order to remove organic molecules on these crystals. The scale bar indicates 25 nm. b) X-ray photoelectron spectroscopy (XPS) analysis of AuNPs synthesised using the B3 peptide. A wide scan and detailed scans of each major region (C 1s, N 1s, and Au 4f) are shown. The dotted and solid lines are the (Shirley) background and peak components, respectively, while the dashed line is the summation of each peak fit and the background.

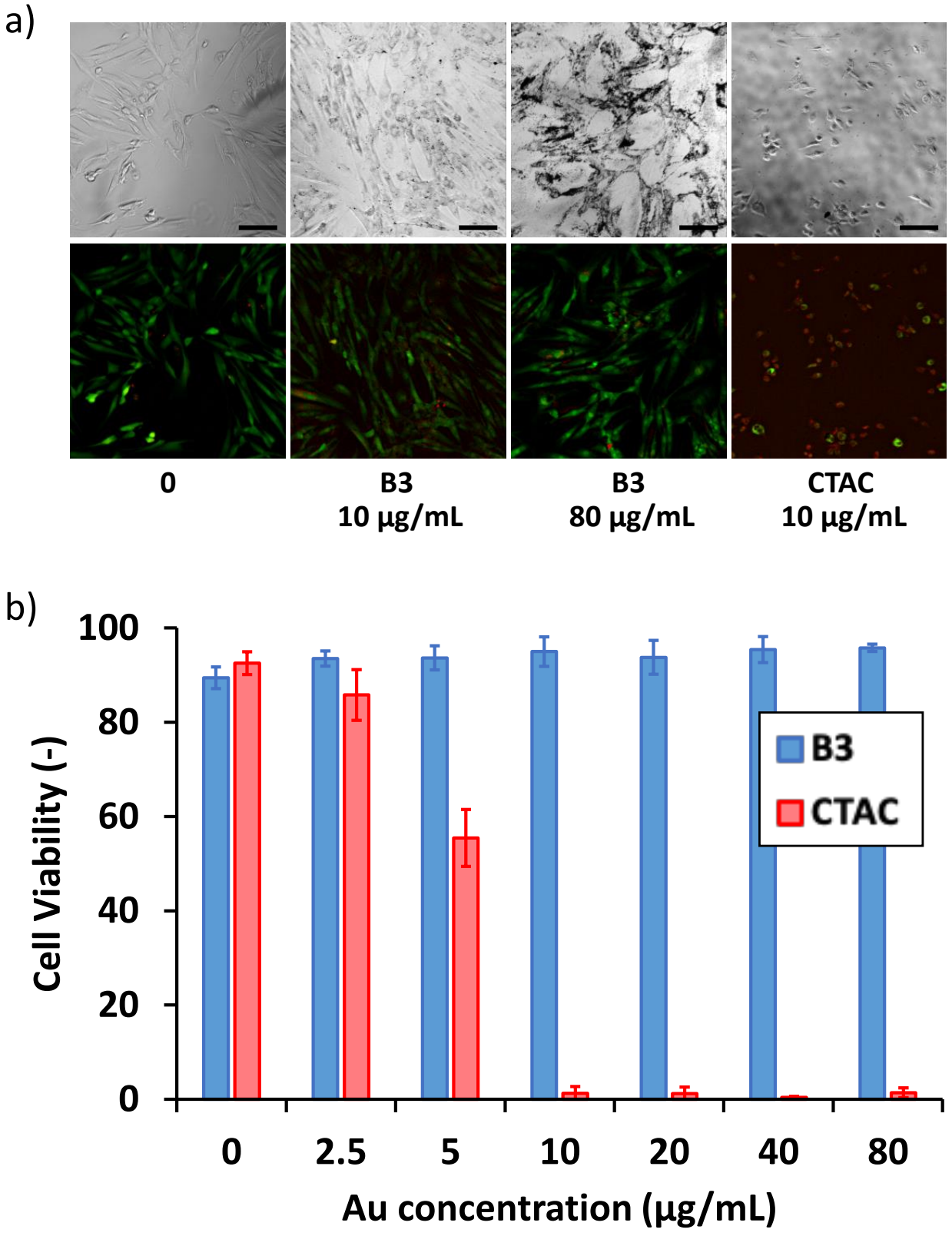

Fig. 5 Effects of B3-AuNPs on the cell viability and cytotoxicity in Normal Human Dermal Fibroblast (NHDF) cell line.

a) Representative bright field and fluorescent images of NHDF which are co-stained with calcein-AM (green) and PI (red) after 0, B3-AuNPs (10 µg/ml), B3-AuNPs (80 µg/ml) and Au nanorod cupped with cetyltrimethylammonium chloride, CTAC (10 µg/ml) exposure for 24 hours. Scale bar shows 100 µm. b) Cell viability was assessed with increasing concentration of B3-AuNPs and CTAC-Au nanorod by manual count of more than 1,000 cells in total in the five fluorescent images. Values were represented as the percentages of cell viability compared with the number of inoculated cells. Error bars were defined as standard deviation (n=5).

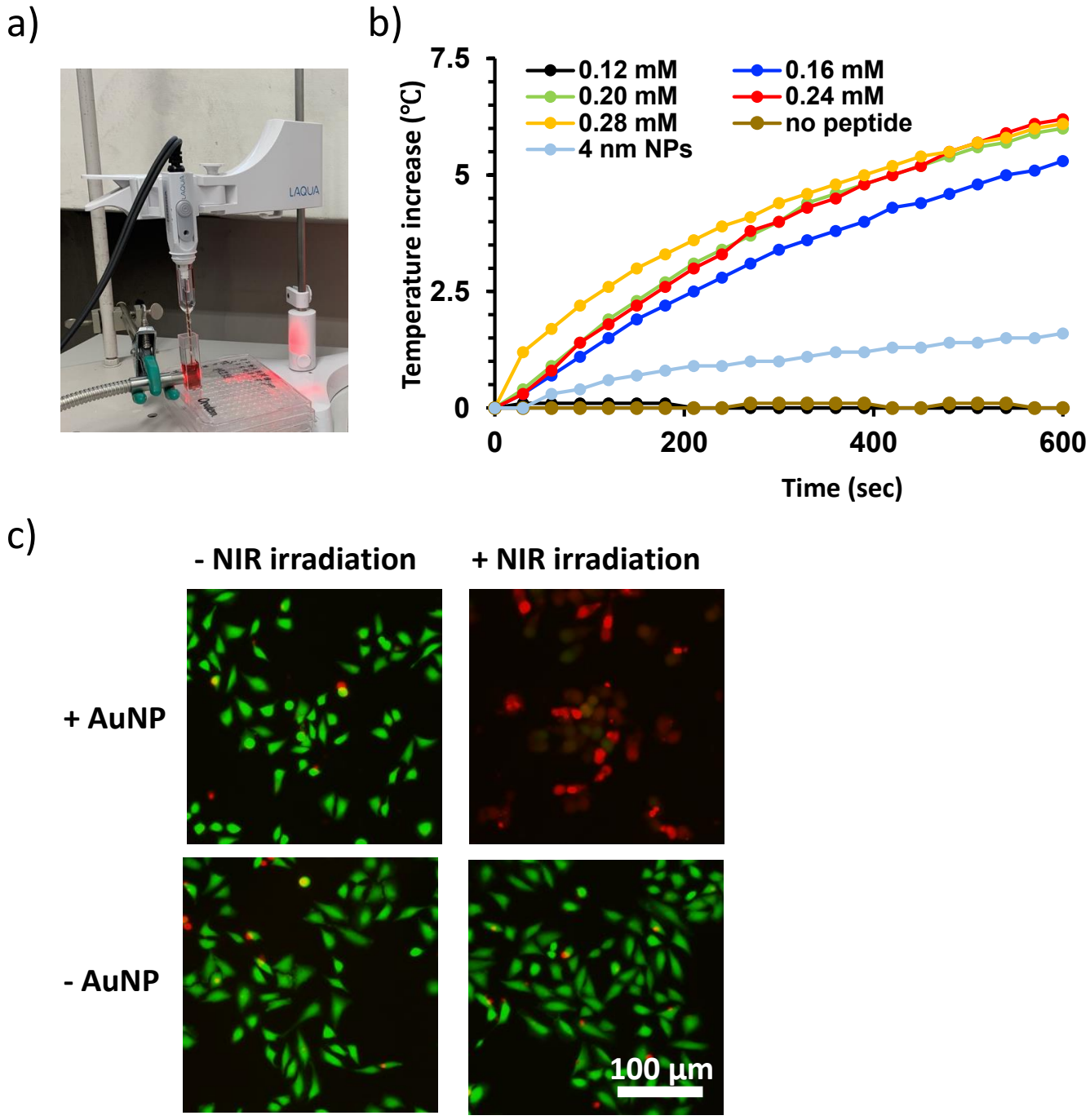

Fig. 6 Evaluation of the photothermal activity of Au nanoparticles synthesised using the B3 peptide.

a) The apparatus used for evaluating the photothermal effect. b) The reaction solution containing Au nanoparticles (AuNPs) synthesised using the B3 peptide at different concentrations (0.12–0.24 mM) was directly irradiated (>610 nm wavelength) and monitored with a thermometer probe. The inset depicts the UV-visible extinction spectrum of the control sample, which is synthesized by the conventional method using $NaBH_4$ as a reducing agent. All syntheses were conducted with a constant concentration of Tris-buffered saline (7 mM) and $HAuCl_4$ (0.5 mM). c) Fluorescence images depicting the phototherapeutic effect of AuNPs synthesised using the B3 peptide (0.25 mM), as assessed by the cell viability assay. Red emission: dead cells and green emission: live cells. Ext., extinction; NP, nanoparticle; AuNP, Au nanoparticle; NIR, near-infrared.

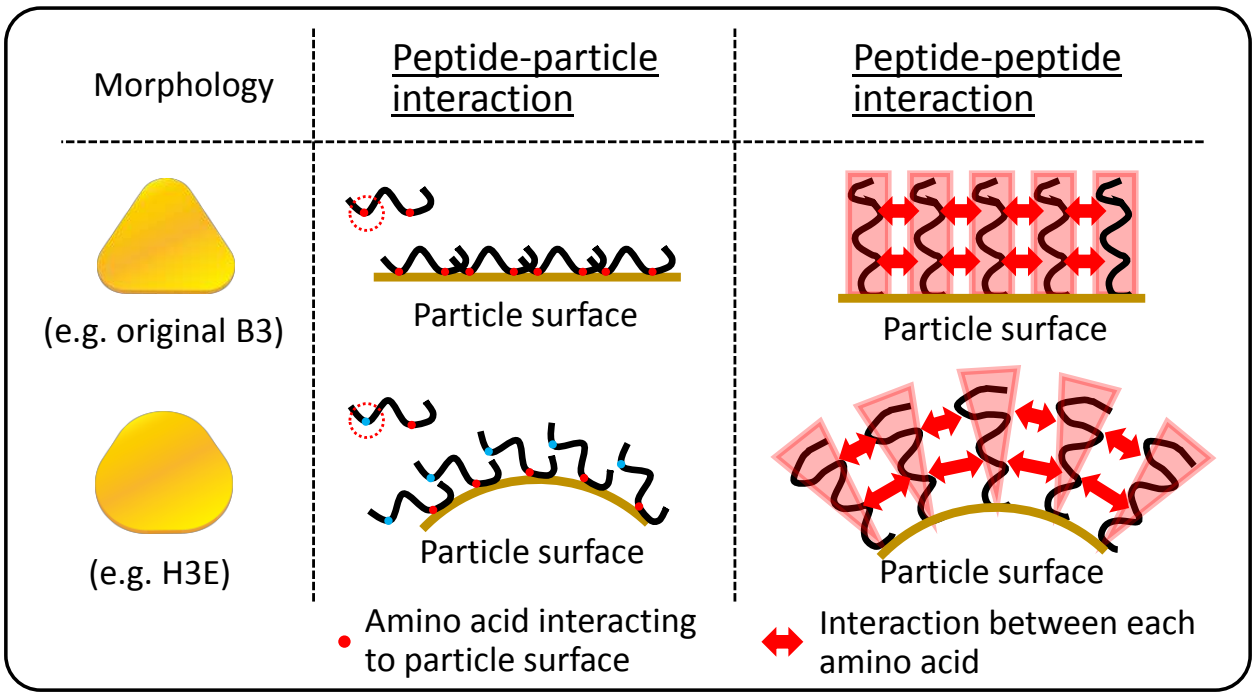

Fig. 7 Proposed models for AuNPls morphological regulation by B3 derivatives.
Through the modification of third amino acid (H) in B3, the morphology of TrAuNPls was changed. From this observation, two possible mechanisms are considered; one is peptide-particle interaction and the other is peptide-peptide interaction.

Supplementary Figure

Supplementary Figure legends

Disclosures

The authors declare that they have no known competing financial interests or personal relationships that could have appeared to influence the work reported in this paper.